CMS Physics Analysis Summary

Contact: cms-pag-conveners-exotica@cern.ch 2017/07/06

Search for dark matter in final states with a top quark and missing transverse momentum using new hadronic top quark tagging techniques

The CMS Collaboration

Abstract

A search for dark matter is conducted in events with large missing transverse momentum and a hadronically decaying, boosted top quark. This study is performed using proton-proton collision data at a center-of-mass energy of $\sqrt{s} = 13$ TeV collected by the CMS detector at the LHC, corresponding to an integrated luminosity of 35.8 fb^{-1}. No significant deviations from standard model predictions are observed, and limits are placed on the production of new heavy bosons coupling to dark matter particles.

1 Introduction

There are strong indications of the existence of dark matter from astrophysical observations [1], which to date are only in the form of gravitational inference. Thus, the nature of dark matter particles has remained elusive. Many searches for dark matter are carried out by looking for interactions between cosmic dark matter and detectors (via nuclear recoil, for example) or for the abundance of particles produced in the annihilation or the decay of cosmic dark matter. The CERN LHC presents a unique opportunity to possibly produce dark matter particles as well as study them. In this paper we describe a search for events where dark matter candidate particles are produced in association with a top quark (dubbed "monotop"). Such searches were originally proposed in Ref. [2] and have been carried out by the CDF Collaboration [3] at the Tevatron and the CMS [4] and ATLAS [5] Collaborations at the LHC. The search presented in this paper utilizes the 13 TeV data set accumulated by the CMS experiment in 2016, corresponding to an integrated luminosity of 35.8 fb^{-1}.

In this search we consider events with a hadronically decaying W boson resulting from the top quark decay. This decay channel has the largest branching fraction and is fully reconstructable. Jets from boosted top quark decays are distinguished from other types of hadronic signatures by use of a novel jet substructure discriminant, described in Section 3.

We interpret the results in terms of two monotop production mechanisms, example Feynman diagrams of which are shown in Fig. 1.

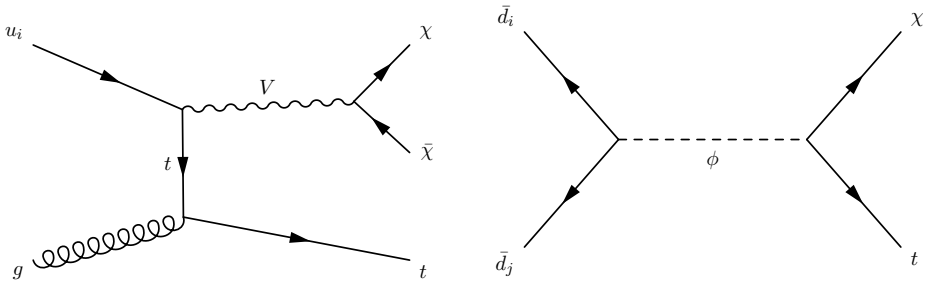

Figure 1: Example of monotop production via a flavor-changing neutral current (left) and a heavy scalar (right).

The first model includes a flavor-changing neutral current, where a top quark is produced in association with a vector boson that has flavor-changing couplings to quarks and can decay to dark matter. It is referred to as the "nonresonant" mode in the following. If we take a simplified model approach, the effective Lagrangian [2, 6, 7] describing nonresonant monotop production is given by:

$$\begin{aligned}\mathcal{L} = \mathcal{L}_{SM} + \mathcal{L}_{kin} + V_\mu \bar{\chi}\gamma^\mu(g_{V_\chi} + g_{A_\chi}\gamma_5)\chi + \text{h.c.} \\ + \bar{q}_u\gamma^\mu(g_{V_u} + g_{A_u}\gamma_5)q_u V_\mu + \bar{q}_d\gamma^\mu(g_{V_d} + g_{A_d}\gamma_5)q_d V_\mu + \text{h.c.}\end{aligned} \tag{1}$$

In Eq. (1), V is the heavy mediator and χ is the dark matter fermion. The couplings g_{V_χ} and g_{A_χ} are the vector- and axial-couplings between χ and V. In the quark-V interaction terms, it is understood that q_u and q_d represent three generations of up- and down-type quarks, respectively. Correspondingly, g_{V_u} and g_{A_u} are 3×3 flavor matrices that control the vector- and axial-couplings between V and u,c,t. It is through the off-diagonal elements of these matrices that monotop production is possible. To preserve SU$(2)_L$ symmetry, analogous down-type couplings g_{V_d} and g_{A_d} must be introduced, and the following must be satisfied:

$$g_{V_u} - g_{A_u} = g_{V_d} - g_{A_d}. \tag{2}$$

By choice, in this paper, we assume $g_{V_u} = g_{V_d}$ and $g_{A_u} = g_{A_d}$, satisfying the above constraint. Moreover, to focus specifically on monotop production, the only nonzero elements of g_{V_u,A_u} are assumed to be those between the first and third generation.

The second model considered contains a colored, charged scalar that decays to a top quark and an invisible fermion χ [7]. In this "resonant" mode the effective Lagrangian is given by:

$$\mathcal{L} = \mathcal{L}_{SM} + \mathcal{L}_{kin}(\phi_s, \chi) + (\phi \bar{d}_i^C [(a_{SR}^q)^{ij} + (b_{SR}^q)^{ij}\gamma^5] d_j + \phi \bar{t}[a_{SR}^{1/2} + b_{SR}^{1/2}\gamma^5]\chi + \text{h.c.}). \quad (3)$$

We assume the couplings a_{SR}^q, b_{SR}^q between ϕ and the quarks to be $a_{SR}^q = b_{SR}^q = 0.1$. Furthermore, for the ϕ-t-χ vertex it is assumed that $a_{SR}^{1/2} = b_{SR}^{1/2} = 0.2$. A more detailed motivation of these conventions is given in Ref. [7].

2 CMS detector

The CMS detector, described in detail in Ref. [8], is a multipurpose apparatus designed to study high-p_T physics processes in proton-proton and heavy ion collisions. A superconducting solenoid occupies its central region, providing a magnetic field of 3.8 T parallel to the beam direction. Charged particle trajectories are measured by the silicon pixel and strip trackers, which cover a pseudorapidity region of $|\eta| < 2.5$. A lead tungstate ($PbWO_4$) crystal electromagnetic calorimeter (ECAL) and a brass/scintillator hadron calorimeter surround the tracking volume and cover $|\eta| < 3$. The steel/quartz-fiber Cherenkov hadron forward calorimeter extends the coverage to $|\eta| < 5$. The muon system consists of gas-ionization detectors embedded in the steel flux return yoke outside the solenoid, and covers $|\eta| < 2.4$. The return yoke facilitates a 2 T return field from the solenoid. The first level of the CMS trigger system is designed to select events in less than 4 μs, using information from the calorimeters and muon detectors. The high-level trigger processor farm then further reduces the event rate to several hundred Hz.

The particle-flow event algorithm [9] reconstructs and identifies each individual particle with an optimized combination of information from the various elements of the CMS detector. The energy of a photon is directly obtained from the ECAL measurement, corrected for zero-suppression effects. The energy of an electron is determined from a combination of the electron momentum at the primary interaction vertex as determined by the tracker, the energy of the corresponding ECAL cluster, and the energy sum of all photons spatially compatible with originating from the electron track. The energy of a muon is obtained from the curvature of the corresponding track. The energy of a charged hadron is determined from a combination of its momentum measured in the tracker and the matching ECAL and HCAL energy deposits, corrected for zero-suppression effects and for the response function of the calorimeters to hadronic showers. Finally, the energy of a neutral hadron is obtained from the corresponding corrected ECAL and HCAL energy.

3 Hadronic Top Quark Identification

If a hadronically decaying top quark is highly boosted, reconstructing the three daughter quarks separately becomes difficult, as the resulting jets will overlap in the detector. Therefore, we employ large cone radius jets ("fat jets") clustered from particle-flow candidate objects to identify such decays. At a transverse momentum (p_T) greater than 250 GeV, the decay products are expected to be within a radius of $\Delta R = 1.5$, where $\Delta R = \sqrt{\Delta\eta^2 + \Delta\phi^2}$. Accordingly, to identify boosted hadronic top quark decays, fat jets are clustered using the Cambridge-Aachen algorithm [10] with a distance parameter of 1.5. To reduce the impact of particles arising from

additional proton-proton interactions (pileup), weights calculated with the PileUp Per Particle Identification (PUPPI) algorithm [11] are applied to the particle-flow candidates. Calibrations derived from data are then applied to correct the absolute scale of the jet energy [12]. Fat jets must pass selection criteria on the transverse momentum ($p_T > 250\,\text{GeV}$) and pseudorapidity ($|\eta| < 2.4$). To identify jets arising from top quark decays, they must have a mass within a range near the top quark mass, have a high likelihood of containing a b quark, and exhibit certain substructure characteristics. Such jets are indicated as "t-tagged" jets hereafter.

In order to define the jet mass, we apply the "soft drop" [13] grooming method, which removes soft and wide angle radiation produced inside a jet by pileup interactions, underlying events, or parton shower activity. The grooming is done with the parameters $z_{cut} = 0.15$, $\beta = 1$, which were chosen to optimize the resolution of the mass after grooming (m_{SD}). We require t-tagged jets to have a soft drop mass in a window of 110–210 GeV in order to be compatible with the top quark mass.

To identify the b quark in the fat jet expected from the top quark decay, we use the combined secondary vertex (CSVv2) algorithm [14, 15]. Soft drop is utilized once again to define "subjets" of the fat jet. The b tagging criterion is then defined by requiring at least one subjet to have a CSVv2 score higher than a particular threshold. The threshold corresponds to correctly identifying a b jet with a probability of 80%, and misidentifying a light-flavor jet with a probability of 10%.

3.1 Substructure

Three classes of substructure observables are employed to distinguish top quark jets from the hadronization products of single light quarks or gluons (hereafter referred to as "q/g jets"). These observables are used as inputs into a boosted decision tree (BDT), which is used as the final discriminator.

N-subjettiness (τ_N) [16] measures the compatibility of a jet with the hypothesis that it is composed of N prongs. For top quark decays, a three-prong topology is expected, while q/g jets may have fewer prongs. This makes the ratio τ_3/τ_2 a robust variable for top quark identification. In this study, the N-subjettiness is computed after jet constituents are removed by soft drop grooming, which reduces the p_T- and mass-dependence of τ_3/τ_2.

The HEPTopTaggerV2 [17] uses the mass-drop and filtering algorithms to construct five subjets of the fat jet. The algorithm then attempts to choose the three subjets that are the most compatible with the top quark decay kinematics. The discriminating variable f_{rec} obtained from this algorithm quantifies the difference between the reconstructed W and top quark masses and their expected values:

$$f_{rec} = \min_{i,j} \left| \frac{m_{ij}/m_{123}}{m_W/m_t} - 1 \right|, \tag{4}$$

where the indices i, j range over the three chosen subjets, m_{ij} is the mass of two subjets, and m_{123} is the mass of all three subjets.

Finally, energy correlation functions (ECFs) e_N are sensitive to correlations among the jet's constituents. A detailed description of ECFs is given in Ref. [18]. They are defined as N-point correlation functions of the constituents' momenta, weighted by the angular separation of the constituents. Discriminating substructure variables are constructed by using ratios of these functions:

$$\frac{{}_a e_N^\alpha}{({}_b e_M^\beta)^x}, \text{ where } M \leq N \text{ and } x = \frac{a\alpha}{b\beta}. \tag{5}$$

In Eq. (5), the six free parameters are $N, a, \alpha, M, b,$ and β. The value of x is chosen to make the ratio dimensionless. As with the N-subjettiness, soft drop grooming is applied to the jet prior to computing the ECFs.

The following ratios of ECFs are found to be able to discriminate between top quark jets and q/g jets, and are therefore considered:

$$\begin{gathered}\frac{{}_1e_2^2}{({}_1e_2^1)^2}, \frac{{}_1e_3^4}{{}_2e_3^2}, \frac{{}_3e_3^1}{({}_1e_3^4)^{3/4}}, \frac{{}_3e_3^1}{({}_2e_3^2)^{3/4}}, \frac{{}_3e_3^2}{({}_3e_3^4)^{1/2}}, \\ \frac{{}_1e_4^4}{({}_1e_3^2)^2}, \frac{{}_1e_4^2}{({}_1e_3^1)^2}, \frac{{}_2e_4^{1/2}}{({}_1e_3^{1/2})^2}, \frac{{}_2e_4^1}{({}_1e_3^1)^2}, \frac{{}_2e_4^1}{({}_2e_3^{1/2})^2}, \frac{{}_2e_4^2}{({}_1e_3^2)^2}.\end{gathered} \tag{6}$$

The final tagger is constructed by training a boosted decision tree using these thirteen variables (τ_3/τ_2, f_{rec}, and the ECF ratios) as inputs. Figure 2 shows the BDT response and performance in discriminating top quark jets from q/g jets. At 50% signal efficiency, the BDT background acceptance is 4.7%, compared to 6.9% for groomed τ_3/τ_2. The BDT response distribution is validated in data as shown in Fig. 3. Control data samples enriched in either true top quark jets from semileptonic $\mathrm{t\bar{t}}$ production or in q/g jets demonstrate a good description of the multivariate tagger.

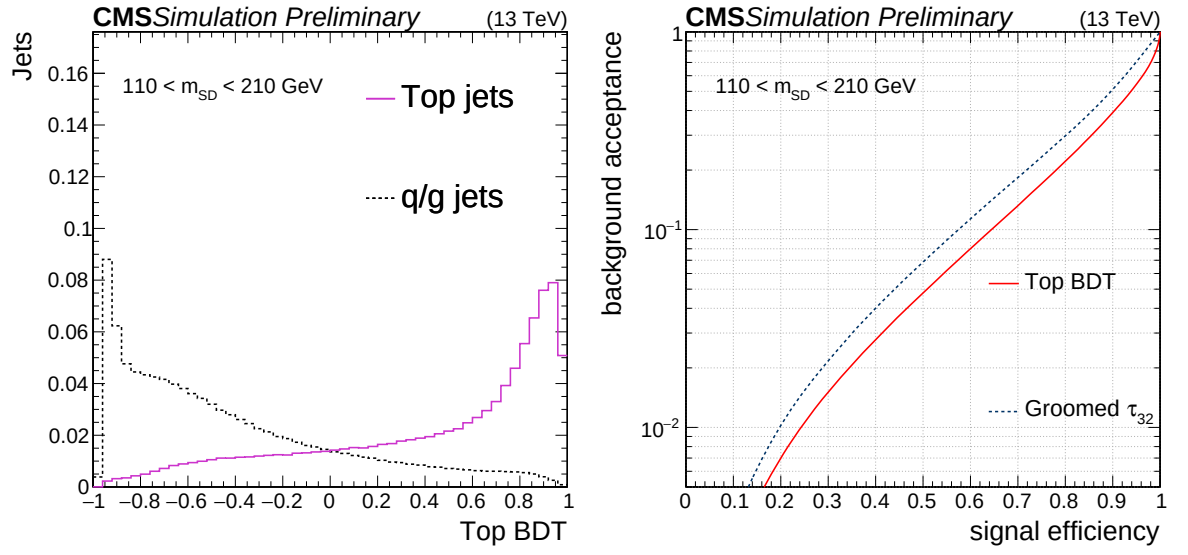

(a) BDT response in top and q/g jets

(b) Comparison of performance of the BDT and τ_3/τ_2

Figure 2: Performance of the top quark tagging BDT in q/g jets and top quark jets. In both figures, the p_{T} spectra of jets are weighted to be flat, and the m_{SD} is required to be in the range 110–210 GeV.

4 Event Selection

4.1 Signal Topology Selection

To search for hadronic monotop production, events are selected with two characteristic signatures: high missing transverse momentum ($p_{\text{T}}^{\text{miss}}$) arising from dark matter candidates and a high-p_{T} fat jet from the decay of a top quark. Events in the signal region are selected by a logical "or" of triggers that require both $E_{\text{T,trig}}^{\text{miss}}$ and $H_{\text{T,trig}}^{\text{miss}}$ to be greater than thresholds of 90, 100,

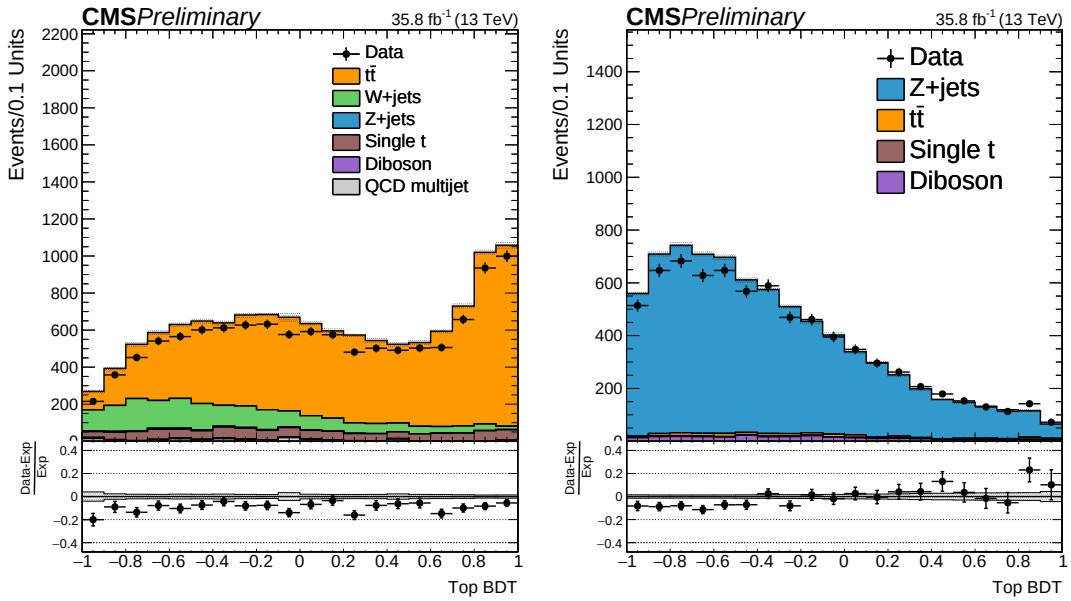

(a) Single muon $t\bar{t}$ selection

(b) $Z \to \mu\mu$ selection

Figure 3: Comparison of the BDT response in data and simulation. The shape of the response is observed to agree well between data and simulation, both in top quark jets and non-top quark jets. The grey band represents the statistical uncertainty of the simulation.

110, or 120 GeV. In the trigger, $E_{\mathrm{T,trig}}^{\mathrm{miss}}$ is calculated as the magnitude of the negative vectorial sum of the p_{T} of all particles at the trigger level and $H_{\mathrm{T,trig}}^{\mathrm{miss}}$ is defined as the negative vectorial sum of the transverse momenta of all jets with p_{T} greater than 20 GeV. While computing $E_{\mathrm{T,trig}}^{\mathrm{miss}}$ and $H_{\mathrm{T,trig}}^{\mathrm{miss}}$, muons are not included in the calculation. Additional selection requirements are imposed on the jets used in the $H_{\mathrm{T,trig}}^{\mathrm{miss}}$ computation in order to remove events resulting from anomalous detector behavior.

In addition to fat jets, this search employs jets clustered using the anti-k_{T} algorithm [19], with a distance parameter of 0.4, having p_{T} larger than 30 GeV and satisfying $|\eta| < 4.7$. These will hereafter be referred to as "jets". The momenta of these jets are corrected to account for mismeasurement of the jet's energy and discrepancies between data and simulation.

The main physics observable in this analysis is $p_{\mathrm{T}}^{\mathrm{miss}}$, defined as the magnitude of the negative vectorial sum $\vec{p}_{\mathrm{T}}^{\mathrm{miss}}$ of the transverse momenta of all final state particles reconstructed using the particle-flow (PF) algorithm [20]. Corrections to the momenta of jets reconstructed in the event are further propagated to the $p_{\mathrm{T}}^{\mathrm{miss}}$. A selected event is required to have $p_{\mathrm{T}}^{\mathrm{miss}} > 250$ GeV. Events with a large misreconstructed $p_{\mathrm{T}}^{\mathrm{miss}}$ are removed by applying beam halo, noise, and bad ECAL super cluster filters. For events passing the analysis selection, the efficiency of the triggers described above is found to be greater than 99%.

To search for events with one hadronic top quark plus missing transverse momentum, exactly one fat jet must be present in the event. As with jets, the momenta of fat jets are corrected. This fat jet must pass the mass and b tagging requirements described in Section 3. To account for discrepancies in b tagging between data and simulation, additional corrections are applied to simulated events. The BDT described in Section 3 is used to split the signal region into two categories. In the loose category, the fat jet is required to have a BDT score greater than 0.1 and

less than 0.45. In the tight category, the minimum BDT score is 0.45.

4.2 Background Rejection

Hadronic monotop events are characterized solely by the signatures described in Section 4.1. Several standard model (SM) processes imitate these characteristics. Events involving pair production of top quarks, in which one top quark decays leptonically and the other hadronically, can have a fat jet from a top quark decay and high $p_{\mathrm{T}}^{\mathrm{miss}}$. Events with $\mathrm{W} \to \ell\nu$ and $\mathrm{Z} \to \nu\nu$ can have large $p_{\mathrm{T}}^{\mathrm{miss}}$ as well, and jets produced in association with the vector bosons can pass the t-tagging selection. To help reject these and other backgrounds, events are vetoed if they contain at least one well identified and isolated electron, muon, tau lepton, or photon. Furthermore, events with an additional b jet that does not overlap with the fat jet are rejected.

A well-identified electron or muon must have $p_{\mathrm{T}} > 10\,\mathrm{GeV}$. Additional criteria are imposed on the ECAL energy deposit, based on the shape of the shower and the presence of a nearby track. To define an isolated electron, the sum of the energies of the particle flow candidates (charged and neutral hadrons and photons) within a cone of $\Delta R < 0.3$ around the electron direction is computed. If this sum is less than 17.5% (15.9%) of the electron's energy and the electron has $|\eta| < 1.479$ ($1.479 < |\eta| < 2.5$), it is considered isolated. Similarly, an isolated muon is defined by looking in a cone of $\Delta R < 0.4$ and setting an energy fraction threshold of 20%. Hadronic tau leptons are required to have $p_{\mathrm{T}} > 18\,\mathrm{GeV}$ and are identified by requiring a jet containing a subset of particles with a mass consistent with the decay products of a hadronic tau lepton. A standard set of identification and isolation criteria is applied to hadronic tau lepton candidates [21]. A photon must have $p_{\mathrm{T}} > 15\,\mathrm{GeV}$ and satisfy criteria on the shape of the shower of the ECAL energy deposit, to distinguish it from an electron or a jet.

We define an isolated jet as a jet that has $\Delta R > 1.5$ with respect to the fat jet. Since isolated jets will solely be used to identify b jets, an isolated jet is further required to satisfy $|\eta| < 2.4$, to remain within the tracker acceptance. To reduce the semileptonic $\mathrm{t\bar{t}}$ background, an event is rejected if there is an isolated jet that is identified as arising from the hadronization of a b quark. The b jets are identified using the same CSVv2 algorithm and working point used to identify b quarks inside a fat jet. As in the case of fat jet b tagging, simulated events are corrected to fix discrepancies in the modeling of isolated jet b tagging. To reduce the background from events with multiple jets produced through the strong interaction (referred to as quantum chromodynamics (QCD) multijet events) in which large $p_{\mathrm{T}}^{\mathrm{miss}}$ arises from mismeasurement of jet momenta, the minimum azimuthal angle between the $\vec{p}_{\mathrm{T}}^{\mathrm{miss}}$ direction and the jets has to be larger than 0.5.

4.3 Monte Carlo Simulation

The dark matter signal is produced with MADGRAPH5_aMC@NLO v2.4.3 [22], where events for the nonresonant production are generated at next-to-leading order (NLO) in QCD; masses for the mediator V above 200 GeV are considered in order to have an SM-like top quark width and avoid decays of the top quark into u plus an on-shell (for $m_V < m_{\mathrm{t}}$) or off-shell (for $m_{\mathrm{t}} \simeq m_V - \Gamma_V$) V boson. The resonant mode is generated at leading-order (LO) accuracy. To model the expectation from SM backgrounds, the $\mathrm{t\bar{t}}$ and single top quark background samples are produced at NLO in QCD using POWHEG v2 [23–25]. Predictions for diboson production are obtained with PYTHIA 8.205 [26].

Simulated samples for the Z+jets, W+jets, γ+jets, and QCD multijet processes are produced with MADGRAPH5_aMC@NLO v2.3.3 at LO and match jets from the matrix element to the parton shower using the MLM prescription [27]. The samples are corrected by weighting the p_{T}

of the respective boson with NLO QCD K factors derived from large MADGRAPH5_aMC@NLO samples, which are generated with the FxFx merging technique [28]. The samples are further corrected by applying NLO electroweak k-factors obtained from theory calculations [29–32] that depend on the boson p_{T}.

All samples (except for diboson production) are interfaced with PYTHIA 8.212 for parton showering, hadronization, and fragmentation. The appropriate LO or NLO NNPDF30 sets [33] are used for obtaining the parametrization of parton distribution functions in all simulations. Interactions of all final state particles with the CMS detector are simulated with GEANT 4 [34].

To model the effect of particles from additional proton-proton interactions in an event, the number of simulated interactions is corrected to match the distribution expected in the data [35].

5 Signal Extraction

A fit of the $p_{\mathrm{T}}^{\mathrm{miss}}$ distribution in the signal region is performed to search for the dark matter signal. After applying the selection described in Section 4, the dominant expected backgrounds are $\mathrm{t\bar{t}}$, $\mathrm{Z}(\nu\nu)+\mathrm{jets}$, and $\mathrm{W}(\ell\nu)+\mathrm{jets}$. These SM processes are estimated using constraints from a simultaneous fit of seven control regions (CRs), which are introduced in Section 5.1. While the requirement on the substructure and mass of the fat jet are the same as in the signal region, the CRs are defined by selections for dimuon, dielectron, γ, single muon (b-tagged and anti-b-tagged), and single electron (b-tagged and anti-b-tagged) events.

In the CRs, the hadronic recoil (U) distribution is used as a proxy to model the $p_{\mathrm{T}}^{\mathrm{miss}}$ distribution in the signal regions. The recoil U is defined by removing leptons or photons (depending on the CR) from the $p_{\mathrm{T}}^{\mathrm{miss}}$ calculation. The primary backgrounds in the signal region are constrained by defining transfer factors from the CRs to the signal region in bins of U. A further description of the transfer factors and their theoretical and experimental uncertainties is given in Sections 5.2 and 5.3. Each CR is split into loose and tight categories, using the same criteria as the signal region categories. Each loose (tight) CR is used to constrain the target background only in the loose (tight) category of the signal region. Single top quark, diboson, and QCD multijet backgrounds are not constrained by a CR and are estimated using Monte Carlo simulation.

A binned likelihood fit is performed simultaneously to the U distributions of data in all signal and control regions. The predictions from the CRs are translated to the signal region through transfer factors that correlate the same bins across all regions employed. These transfer factors are allowed to vary within uncertainties as described in Section 5.3.

5.1 Control regions

To estimate $\mathrm{Z}(\nu\nu)+\mathrm{jets}$ in the signal region, CRs enriched in dimuon, dielectron, and photon events are used.

Dimuon events are selected online employing the same $E_{\mathrm{T,trig}}^{\mathrm{miss}}$ triggers that are used in the signal region, since these triggers do not include muons in the $E_{\mathrm{T,trig}}^{\mathrm{miss}}$ calculation. These events are required to have two opposite-charge muons having p_{T} greater than 10 GeV that form an invariant mass between 60 GeV and 120 GeV. At least one of the two muons must have p_{T} greater than 20 GeV and pass tight identification and isolation requirements. Events in the dimuon region must also pass almost all other selection requirements imposed on the events in the signal region, wherein U is substituted for $p_{\mathrm{T}}^{\mathrm{miss}}$. In order to increase the number of events in the dimuon CR, the requirement of the fat jet b tag is not imposed.

Dielectron events are selected online using single electron triggers, which have a p_T threshold of 27 GeV. Two opposite-charge electrons with p_T greater than 10 GeV are required, and they must form an invariant mass between 60 GeV and 120 GeV. To be on the plateau of the trigger efficiency, at least one of the two electrons must have $p_T > 40$ GeV and satisfy tight identification and isolation requirements. All selection criteria applied in the dimuon CR are applied in the dielectron CR.

The γ + jets control sample is constructed using events with at least one high-p_T photon. A single-photon trigger with a p_T threshold of 165 GeV is used to select these events. The photon p_T is required to be greater than 175 GeV in order to ensure that the trigger is maximally efficient. The photon candidate is required to pass identification and isolation criteria, and is further required to be reconstructed in the ECAL barrel ($|\eta| < 1.44$) to obtain a high purity of 95% [36]. As in the dilepton regions, the fat jet b tag requirement is not applied in the photon region.

Events that enter the signal selection due to the loss of a single lepton primarily arise from $W(\ell\nu)$ + jets and semileptonic $t\bar{t}$ events. To estimate these backgrounds, four single-lepton samples are used: single muon and single electron, b-tagged and anti-b-tagged. The b-tagged single lepton CRs are enhanced in $t\bar{t}$ events, while the anti-b-tagged single lepton CRs target $W(\ell\nu)$ + jets events.

Single muon events are selected using the $E_{T,trig}^{miss}$ trigger. The muon candidate in these events is required to have p_T greater than 20 GeV, and is required to be well identified and isolated. With the exception of b tagging, all other selection requirements used for signal events are imposed, using U instead of p_T^{miss}. In addition, to suppress QCD multijet events, the transverse mass (M_T) is required to be less than 160 GeV, where $M_T = \sqrt{2p_T^{miss}p_T^{\ell}(1-\cos\Delta\phi(\vec{p}_T^{miss}, p_T^{\ell}))}$. In the b-tagged single muon CR, we require (a) the fat jet to be b-tagged as in the signal region and (b) exactly one b-tagged isolated jet. In the anti-b-tagged single muon CR, the b tagging requirements are reversed, so that the fat jet is not b-tagged and there are exactly zero b-tagged isolated jets.

The single electron CRs are defined similarly to the single muon CRs. Events are selected using the single electron trigger and the p_T of the electron is required to be greater than 40 GeV. An additional requirement of $p_T^{miss} > 50$ GeV is imposed on single electron events in order to suppress the QCD multijet background.

A summary of the selection criteria for the signal region and for all control regions is given in Table 1.

To account for discrepancies between data and simulation in the efficiencies of identifying electrons, muons, and photons, correction factors are applied to simulated events in regions where these objects are selected.

5.2 Transfer Factors

The dominant SM process in each CR is used to estimate at least one background in the signal region. Each constraint is encoded through a transfer factor R, which is the ratio of the expected yield of the target process in the signal region and its expected yield in the CR. As described in Section 4.3, R is defined as a function of U and is estimated using simulation. If the CR X is used to estimate the process Y in the signal region, and μ_i^Y is the free parameter of the likelihood representing the number of events observed in bin i of U in the signal region, then

Table 1: Summary of the selection criteria used in the signal and CRs. Symbols (b) and (ℓ) respectively refer to cases where the b-quark and lepton are not identified. N_e, N_μ, and N_γ refer to the number of selected electrons, muons, and photons, respectively. The number of b-tagged narrow jets that are isolated from the fat jet are denoted with $N^{\text{iso}}_{\text{b-tag}}$.

Region(s)	Main process(es)	N_e	N_μ	N_γ	$N^{\text{iso}}_{\text{b-tag}}$	Fat jet b-tag
Signal	$W \to (\ell)\nu$, $Z \to \nu\nu$, $t\bar{t} \to (b)qq' + b(\ell)\nu$	0	0	0	0	1
Single-e (b-tagged)	$t\bar{t} \to bqq' + be\nu$	1	0	0	1	1
Single-μ (b-tagged)	$t\bar{t} \to bqq' + b\mu\nu$	0	1	0	1	1
Single-e (anti-b-tagged)	$W \to e\nu$	1	0	0	0	0
Single-μ (anti-b-tagged)	$W \to \mu\nu$	0	1	0	0	0
Dielectron	$Z \to ee$	2	0	0	0	–
Dimuon	$Z \to \mu\mu$	0	2	0	0	–
Photon	γ	0	0	1	0	–

the expected number of events N_i^X in the CR is given by $N_i^X = \dfrac{\mu_i^\gamma}{R_i^X}$.

The $t\bar{t}$ and W+jets backgrounds in the signal region are estimated using data in the corresponding subsample of the single lepton CRs. Transfer factors (R^ℓ and $R^{b\ell}$) are derived from simulations that take into account the impact of lepton acceptances and efficiencies, the b-tagging efficiency, and, for the single electron control sample, the additional $p_{\text{T}}^{\text{miss}}$ requirement. This transfer factor explicitly includes hadronic tau leptons that fail the hadronic tau lepton identification criteria, which account for roughly 20-80% of the total W+jets background in the high recoil region. Because of a large $t\bar{t}$ contamination in the tight W+jets CR, an additional transfer factor is imposed between the $t\bar{t}$ in the b-tagged and anti-b-tagged single-lepton CRs. This allows an estimation of the $t\bar{t}$ contribution in both the signal region and W+jets CRs to be made from the b-tagged CR.

The $Z(\nu\nu) + \text{jets}$ background prediction in the signal region is connected to the dimuon and dielectron CRs through transfer factors ($R^{\ell\ell}$). They are derived using simulation and account for the difference in the branching fractions of $Z \to \nu\nu$ and $Z \to \ell\ell$ decays and the impacts of lepton acceptances and selection efficiencies. Since the branching fraction of the Z boson decaying to electrons and muons is roughly three times smaller than that to neutrinos, the resulting constraint on the $Z(\nu\nu) + \text{jets}$ background from the dilepton CRs is limited by the statistical uncertainty in the dilepton control samples at large values of U.

The $\gamma + \text{jets}$ CR is also used to constrain the $Z(\nu\nu) + \text{jets}$ background prediction via a transfer factor R^γ, which accounts for the difference in cross section and the acceptance and efficiency of identifying the photon events. This production mode has a similar initial state to $Z(\nu\nu) + \text{jets}$, allowing for a constraint from data on the shape of the predicted Z p_{T} spectrum. Since the production cross section of $\gamma + \text{jets}$ events is roughly twice that of $Z(\nu\nu) + \text{jets}$ events, the addition of this CR to constrain the $Z(\nu\nu) + \text{jets}$ background prediction reduces the impact of the limited statistical power of the dilepton events. However, additional theoretical systematic uncertainties are introduced while extrapolating from this CR to the signal region.

A further constraint on the $Z(\nu\nu) + \text{jets}$ background prediction is given by W+jets events in the single-lepton anti-b-tagged CRs via $R^{W/Z}$ transfer factors. Additional theoretical uncertainties

are considered to cover the extrapolation from $\mathrm{W}(\ell\nu) + \text{jets}$ to $\mathrm{Z}(\nu\nu) + \text{jets}$ events.

5.3 Systematic Uncertainties

The U spectra of the $\mathrm{t\bar{t}}$, W, and Z backgrounds are determined through a binned maximum likelihood fit, performed simultaneously across all fourteen CRs and two signal regions.

Systematic uncertainties are treated as constrained nuisance parameters, $\boldsymbol{\theta}$, which allow for variation of the transfer factors R^X. These include theoretical uncertainties on the γ/Z and W/Z differential cross section ratios from the choice of the renormalization and factorization scales, as well as the parton distribution function (PDF) uncertainty following the NNPDF3.0 [33] prescription. Systematic uncertainties due to higher order electroweak corrections to the γ, W and Z differential cross sections are estimated by taking the full NLO electroweak correction as a function of boson p_{T} as an uncertainty.

An uncertainty of 21% on the heavy flavor fraction of W+jets is computed using CMS measurements of inclusive W+jets [37] and W+heavy flavor [37, 38] production. This uncertainty is then propagated to each of the signal and CRs by varying the heavy flavor fraction up and down in the Monte Carlo prediction. These W+heavy flavor fraction uncertainties are correlated between all regions in the fit. A similar method is used for the Z+heavy flavor fraction uncertainty (22%) using measurements of Z+jets production at CMS [39, 40]. This uncertainty is also correlated between all regions, but is uncorrelated with the W+heavy flavor nuisance. The magnitudes of these W/Z+heavy flavor uncertainties are different for each region (depending on the b tagging requirements) and range from 2% to 4% of the nominal W/Z+jets prediction.

We propagate uncertainties in the efficiencies of b tagging jets and subjets as shape uncertainties in the distribution of U.

Additional uncertainties are included to account for the differences between data and simulation when applying a t-tagging selection. To evaluate the uncertainty for top quark jets, first the efficiency of the t-tag is measured in data using the mass spectrum of fat jets in $\mathrm{t\bar{t}}$ events, where one top quark decays to a muon. Then, variations due to parton shower algorithm, higher-order corrections, and experimental effects are propagated to the efficiency measurement. These result in a final uncertainty for tagging fat jets from a top quark decay of 6%. Similarly, the uncertainty in mistagging a non-top quark jet is measured by computing the efficiency for a $Z(\mu\mu)$+jets selection. The mistag uncertainty is 7%. These variations are included in the fit as rate uncertainties.

Uncertainties in the selection efficiencies amount to 1% per selected muon, electron, or photon, while the uncertainty in the tau lepton veto is 3%; these are correlated across all U bins. A systematic uncertainty of 20% is ascribed to the single top quark background prediction [41] and is correlated between the signal region and the leptonic CRs. An uncertainty of 20% is assigned to the diboson production cross section [42, 43] and correlated across all channels.

The QCD multijet background is estimated from Monte Carlo simulation in all regions except for the γ+jets CR, where the prediction is obtained from data by applying a jet-to-photon misidentification probability measured in an orthogonal control sample. An uncertainty of 100% is used for the overall QCD multijet yield. This is estimated using a sample enriched in QCD multijet events, obtained by requiring the minimum azimuthal angle between $\vec{p}_{\mathrm{T}}^{\,\mathrm{miss}}$ and the jet directions to be less than 0.1.

For processes estimated from Monte Carlo simulation, $p_{\mathrm{T}}^{\mathrm{miss}}$ uncertainties are obtained directly from simulation and propagated to U following the standard CMS method [44], which in-

cludes the jet energy correction uncertainties applied to the jets and the $p_{\mathrm{T}}^{\mathrm{miss}}$ [12]. The $p_{\mathrm{T}}^{\mathrm{miss}}$ uncertainty is included as a rate uncertainty in the final fit.

A systematic uncertainty of 2.5% in the luminosity measurement [35] is included for all the processes that are estimated using Monte Carlo simulation.

An uncertainty of 10% (20%) is assigned to the inclusive nonresonant (resonant) signal cross sections. This includes the renormalization and factorization scale uncertainties, and the PDF uncertainties.

6 Results

Figures 4–7 show the result of the simultaneous fit in all fourteen control regions. Good agreement is observed in all control regions.

Figure 8 shows the distribution of $p_{\mathrm{T}}^{\mathrm{miss}}$ in the signal region after the fit is performed under the background-only hypothesis. Data are found to be in agreement with the SM prediction.

The results of the search are first interpreted in terms of a simplified model for monotop production via a flavor-changing neutral current (FCNC). Expected and observed limits at 95% confidence level (CL) are shown in Fig. 9 and are set using the Asymptotic CLs method [45] with a profile likelihood ratio as the test statistic, in which systematic uncertainties are modeled as nuisance parameters. Assuming couplings of $g_{V_u} = 0.25$ and $g_{V_\chi} = 1$, the flavor-changing neutral current is excluded for mediator masses of $0.2 < m_V < 1.75\,\mathrm{TeV}$, assuming a DM fermion mass of 1 GeV. This is compared to an expected exclusion of $0.2 < m_V < 1.78\,\mathrm{TeV}$.

In addition to scanning the dark matter and mediator masses, the analysis interprets the results as a function of the couplings between dark matter and the mediator, and between quarks and the mediator. Figure 10 shows the 95% CL exclusion in the planes spanned by these parameters. At low mediator and DM masses, coupling combinations as small as $g_{\mathrm{DM}} = 0.2, g_q = 0.25$ and $g_{\mathrm{DM}} = 1, g_q = 0.05$ are excluded.

Figure 11 shows the results in the resonant interpretation. Scalars of mass $m_\phi < 3.4\,\mathrm{TeV}$ are excluded at 95% CL.

7 Summary

A search for dark matter in the monotop final state is performed. The data are found to be in agreement with the standard model prediction. Results are interpreted in terms of limits on the production cross section of dark matter particles via a neutral flavor-changing interaction or via the decay of a colored, scalar resonance together with a single top quark.

For the nonresonant model, assuming $m_\chi = 1$ GeV, $g_{V_u} = 0.25$, and $g_{V_\chi} = 1$, flavor-changing neutral currents of $m_V < 1.75\,\mathrm{TeV}$ are excluded at 95% confidence level.

For the resonant model, scalar fields with $m_\phi < 3.4\,\mathrm{TeV}$ are excluded.

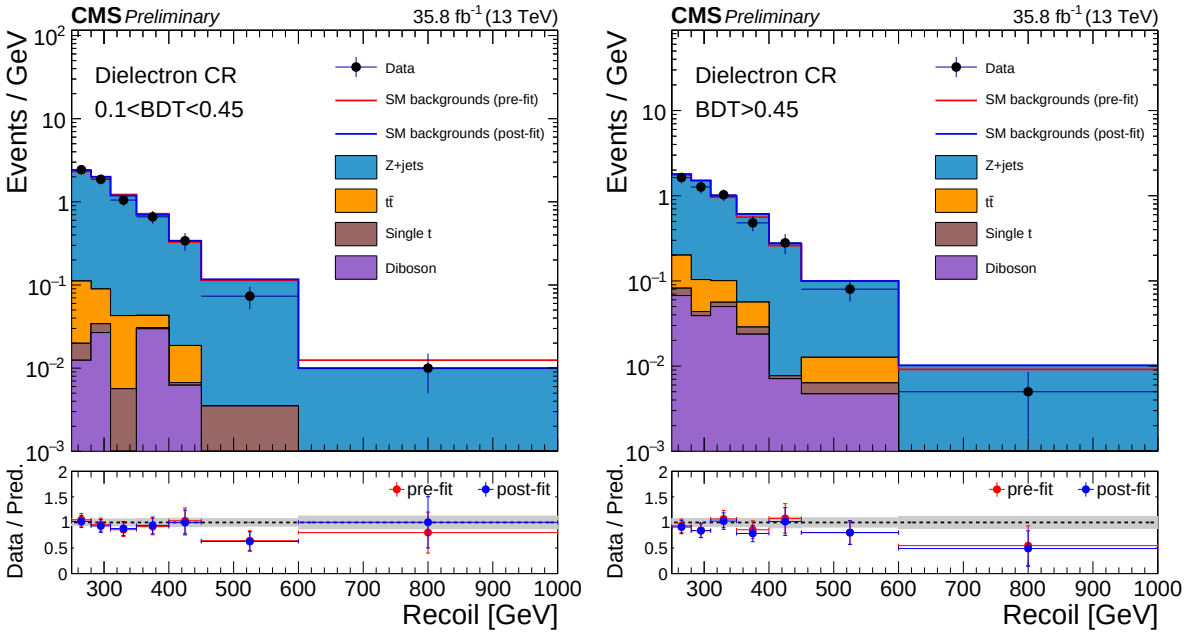

(a)

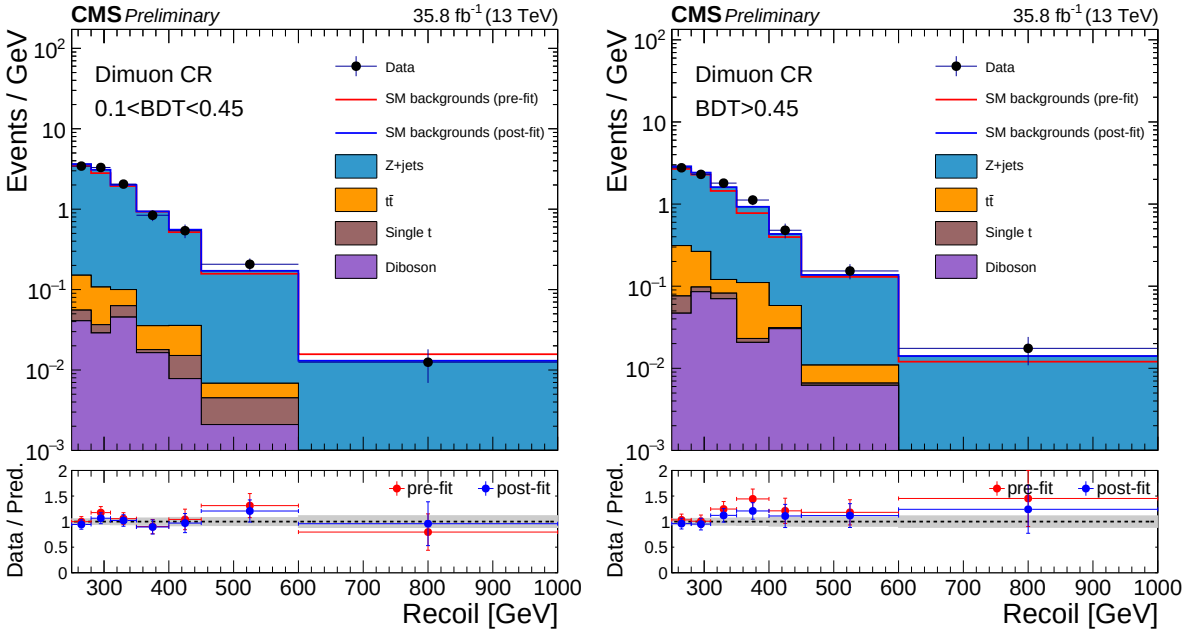

(b)

Figure 4: Comparison between data and SM predictions in the control regions before and after performing the simultaneous fit to the different control regions and signal region. Each bin shows the event yields divided by the width of the bin. Plot (a) corresponds to the dielectron control region, and plot (b) corresponds to the dimuon control region. The blue solid line represents the sum of the SM background contributions normalized to their post-fit yields. The red solid line represents the sum of the SM background contributions normalized to the theoretical prediction. The stacked histograms show the individual SM background distributions after the fit is performed. The gray band indicates the post-fit uncertainty after propagating all the systematic uncertainties in the fit.

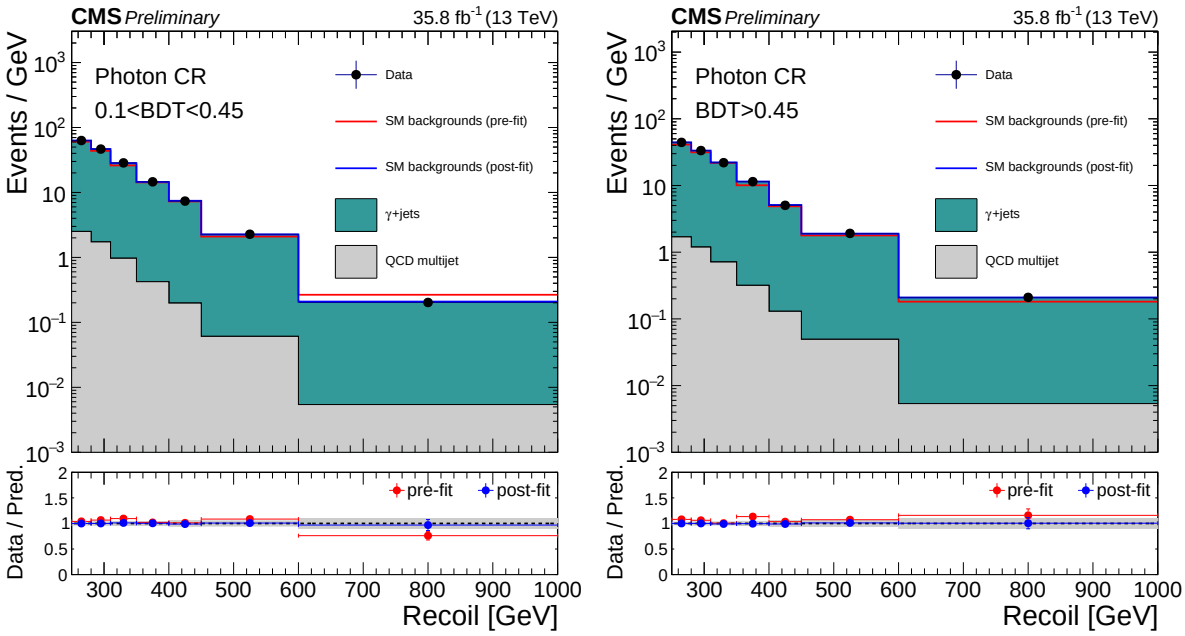

Figure 5: Comparison between data and SM predictions in the photon control regions before and after performing the simultaneous fit to the different control regions and signal region. Each bin shows the event yields divided by the width of the bin. The blue solid line represents the sum of the SM background contributions normalized to their post-fit yields. The red solid line represents the sum of the SM background contributions normalized to the theoretical prediction. The stacked histograms show the individual SM background distributions after the fit is performed. The gray band indicates the post-fit uncertainty after propagating all the systematic uncertainties in the fit.

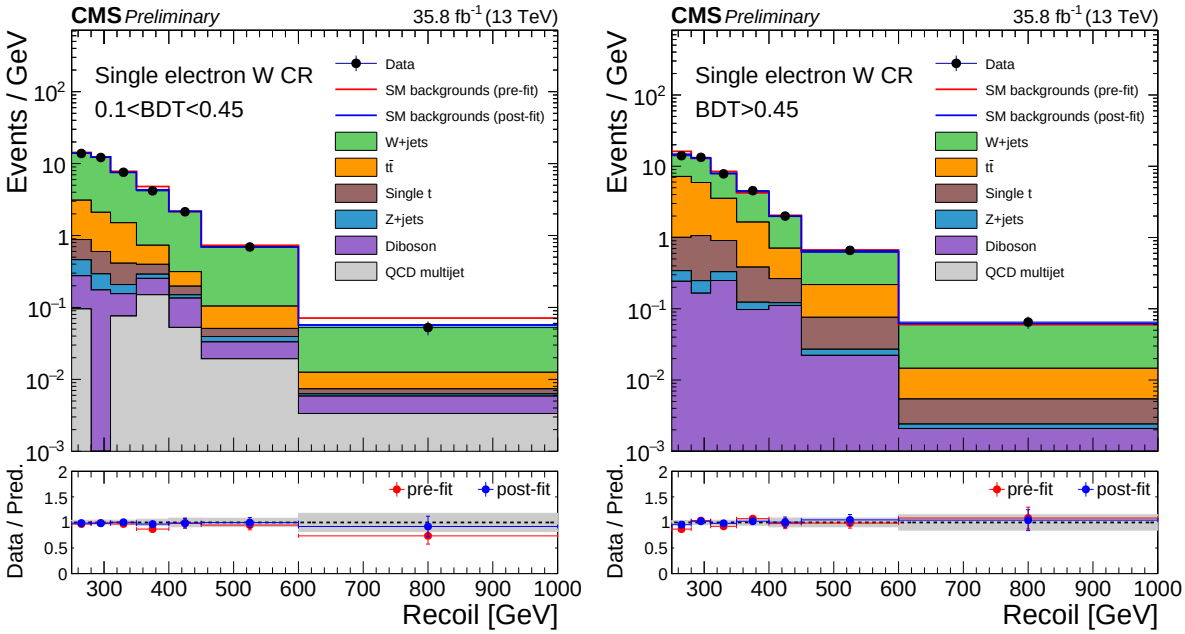

(a)

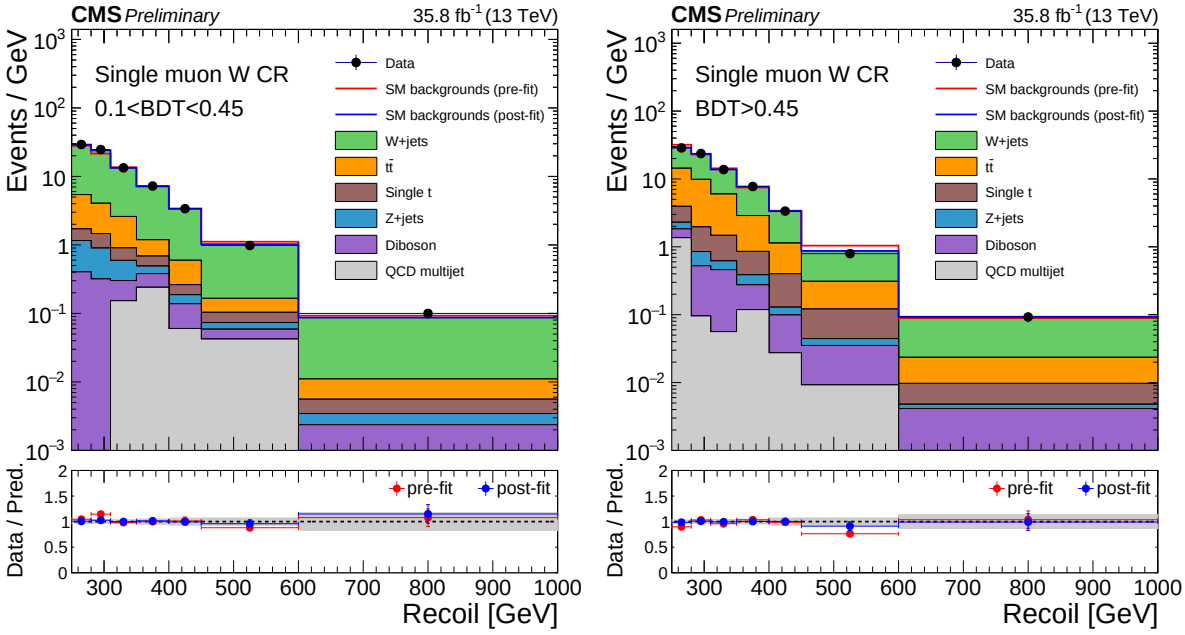

(b)

Figure 6: Comparison between data and SM predictions in the control regions before and after performing the simultaneous fit to the different control regions and signal region. Each bin shows the event yields divided by the width of the bin. Plot (a) corresponds to the single electron anti-b-tagged control region and plot (b) corresponds to the single muon anti-b-tagged control region. The blue solid line represents the sum of the SM background contributions normalized to their post-fit yields. The red solid line represents the sum of the SM background contributions normalized to the theoretical prediction. The stacked histograms show the individual SM background distributions after the fit is performed. The gray band indicates the one standard deviation uncertainty on the prediction that also includes systematic uncertainties.

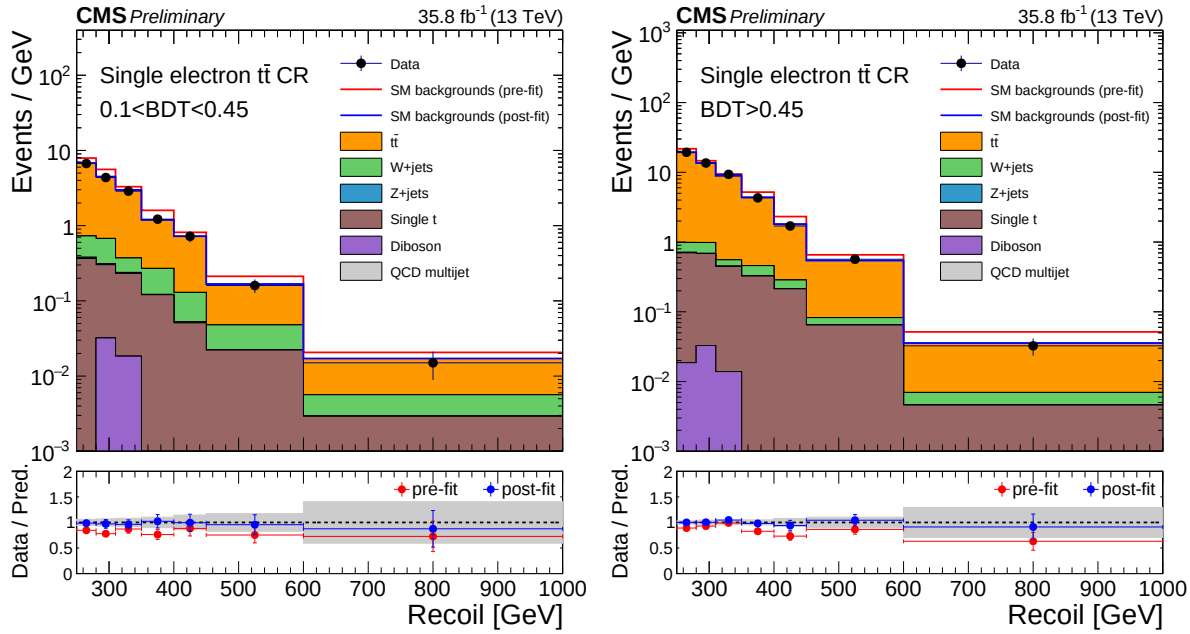

(a)

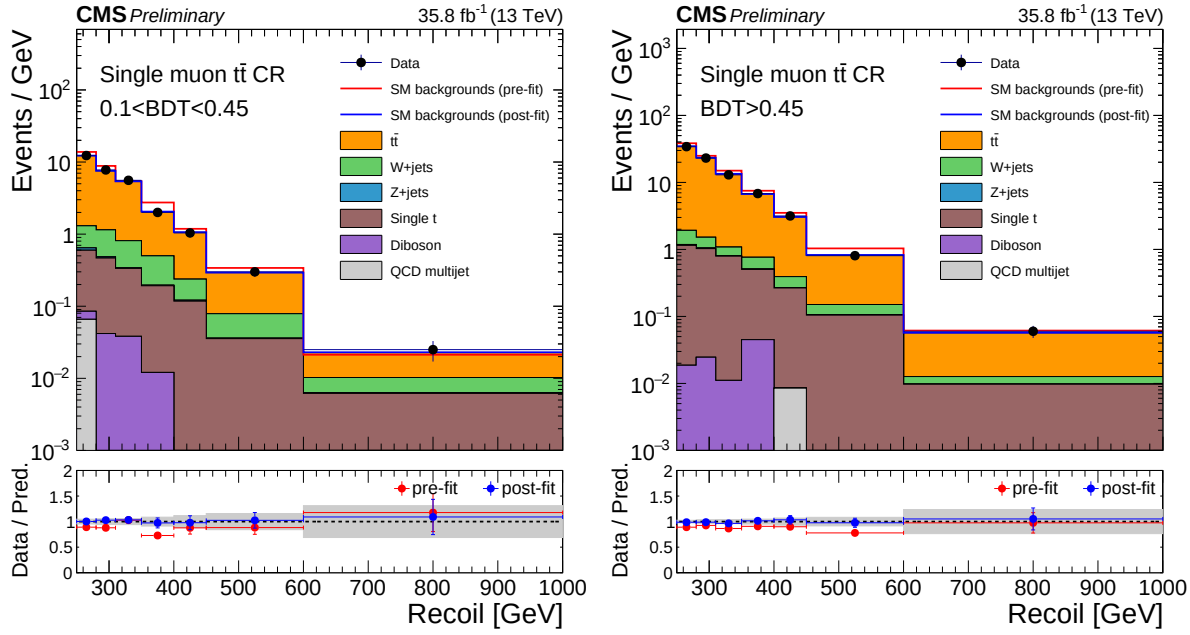

(b)

Figure 7: Comparison between data and SM predictions in the control regions before and after performing the simultaneous fit to the different control regions and signal region. Each bin shows the event yields divided by the width of the bin. Plot (a) corresponds to the single electron b-tagged control region and plot (b) corresponds to the single muon b-tagged control region. The blue solid line represents the sum of the SM background contributions normalized to their post-fit yields. The red solid line represents the sum of the SM background contributions normalized to the theoretical prediction. The stacked histograms show the individual SM background distributions after the fit is performed. The gray band indicates the post-fit uncertainty after propagating all the systematic uncertainties in the fit.

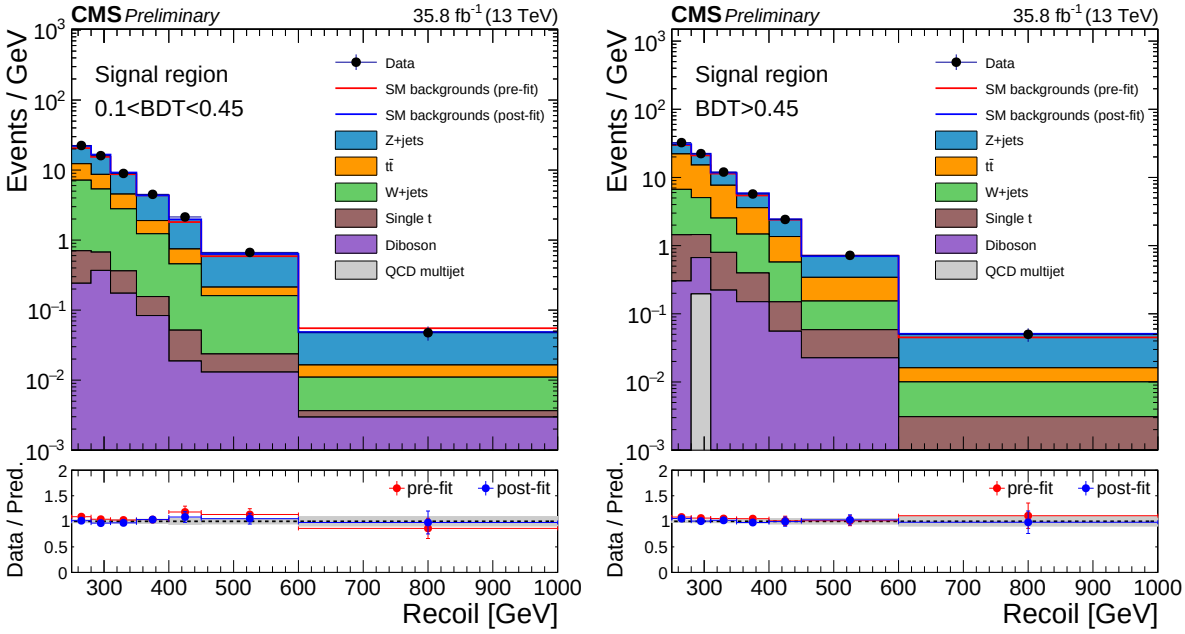

Figure 8: Distribution of $p_{\mathrm{T}}^{\mathrm{miss}}$ from SM backgrounds and data in the signal region after simultaneously fitting in the signal region and all control regions. Each bin shows the event yields divided by the width of the bin. The stacked histograms show the individual SM background distributions after the fit is performed. The blue solid line represents the sum of the SM background contributions normalized to their post-fit yields. The red solid line represents the sum of the SM background contributions normalized to the theoretical prediction. The gray bands indicate the post-fit uncertainty in the background, assuming no signal.

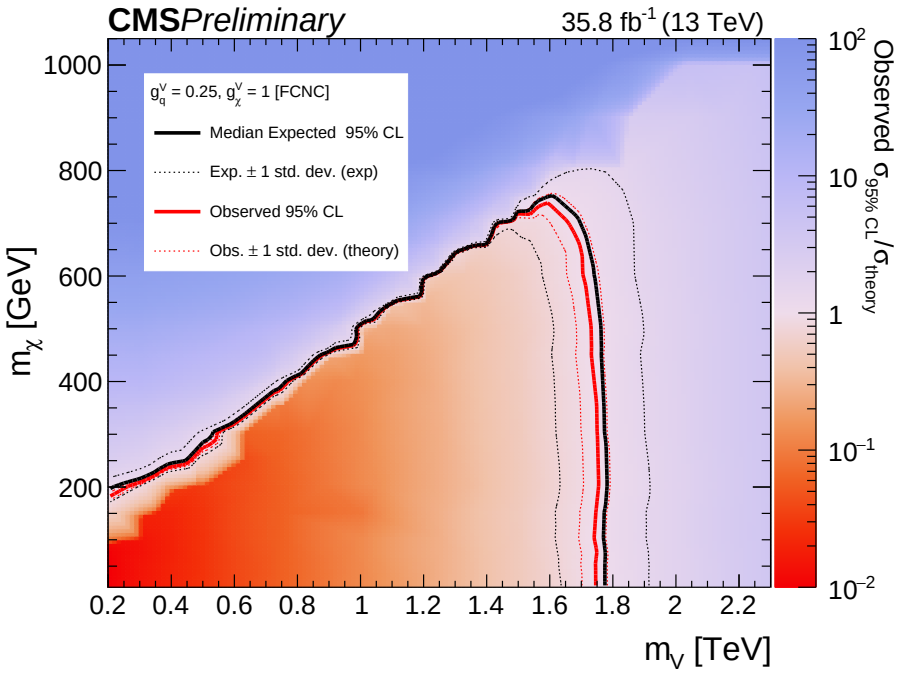

Figure 9: Results for the FCNC interpretation presented in the two-dimensional plane spanned by the mediator and dark matter masses. The mediator is assumed to have purely vector couplings to quarks and dark matter. The observed exclusion range (red solid line) is shown. The red dashed lines show the cases in which the predicted cross section is shifted by the assigned theory uncertainty. The expected exclusion range is indicated by a black solid line, demonstrating the search sensitivity of the analysis. The experimental uncertainties are shown in black dashed lines.

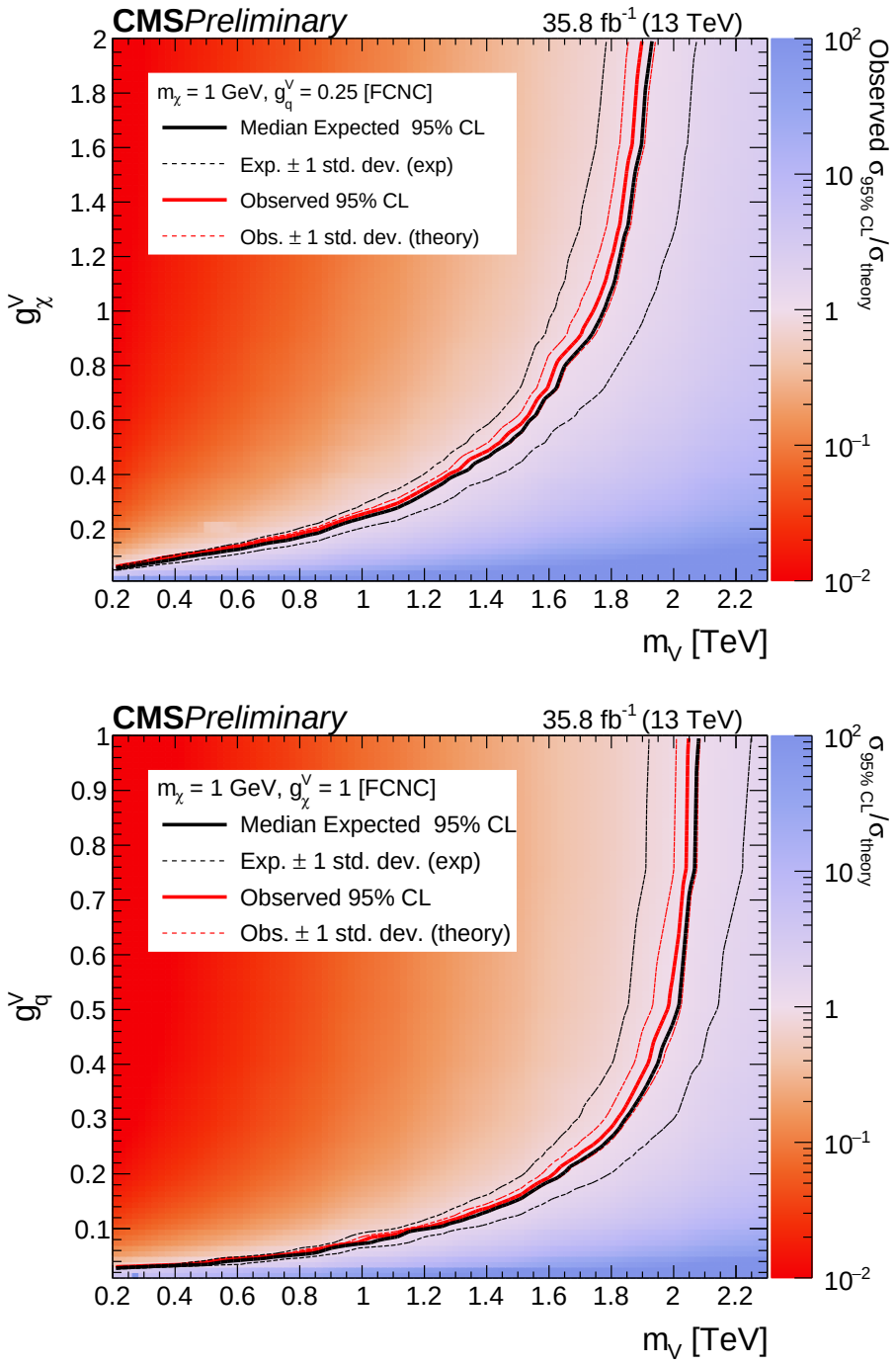

Figure 10: Results for the FCNC interpretation presented in the two-dimensional plane spanned by the mediator mass and the coupling between the mediator and dark matter (top) or quarks (bottom). The mediator is assumed to have purely vector couplings. The observed exclusion range (red solid line) is shown. The red dashed lines show the cases in which the predicted cross section is shifted by the assigned theory uncertainty. The expected exclusion range is indicated by a black solid line, demonstrating the search sensitivity of the analysis. The experimental uncertainties are shown in black dashed lines.

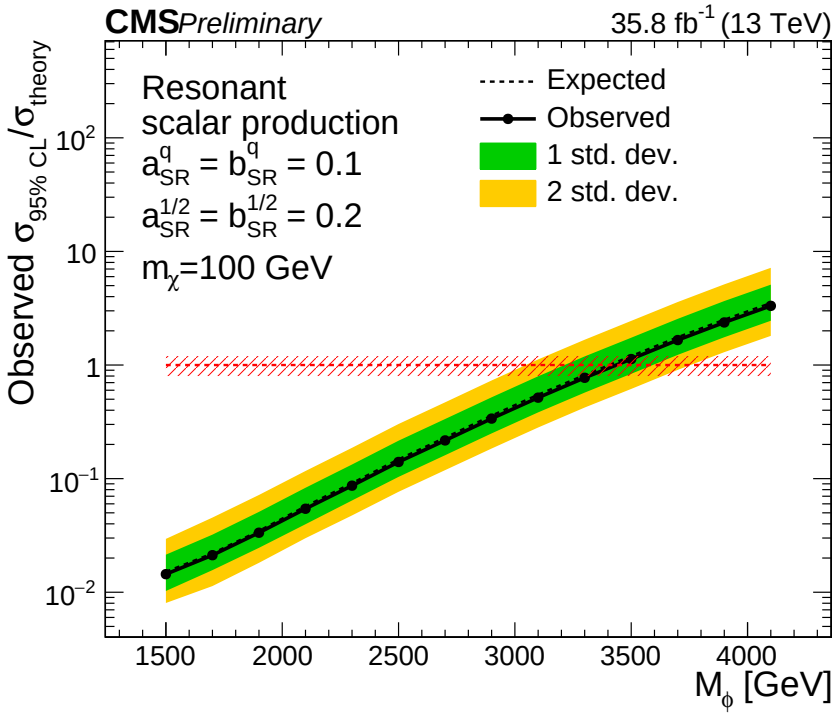

Figure 11: Results assuming a resonant interpretation of the monotop signature. Shown are upper limits as a function of the mass of the scalar particle S, assuming fixed $a_{\mathrm{SR}} = b_{\mathrm{SR}} = 0.1$. The limits are placed at a confidence level of 95%. The green and yellow bands represent one and two standard deviations of experimental uncertainties, respectively. The red shaded band represents the 20% signal cross section uncertainty.

References

[1] LUX Collaboration, "Improved Limits on Scattering of Weakly Interacting Massive Particles from Reanalysis of 2013 LUX Data", *Phys. Rev. Lett.* **116** (2016) 161301, doi:10.1103/PhysRevLett.116.161301, arXiv:1512.03506.

[2] J. Andrea, B. Fuks, and F. Maltoni, "Monotops at the LHC", *Phys. Rev.* **D84** (2011) 074025, doi:10.1103/PhysRevD.84.074025, arXiv:1106.6199.

[3] CDF Collaboration, "Search for a Dark Matter Candidate Produced in Association with a Single Top Quark in $p\overline{p}$ Collisions at $\sqrt{s} = 1.96$ TeV", *Phys. Rev. Lett.* **108** (2012) 201802, doi:10.1103/PhysRevLett.108.201802, arXiv:1202.5653.

[4] CMS Collaboration, "Search for Monotop Signatures in Proton-Proton Collisions at $\sqrt{s} = 8$ TeV", *Phys. Rev. Lett.* **114** (2015) 101801, doi:10.1103/PhysRevLett.114.101801, arXiv:1410.1149.

[5] ATLAS Collaboration, "Search for invisible particles produced in association with single-top-quarks in proton-proton collisions at $\sqrt{s} = 8$ TeV with the ATLAS detector", *Eur. Phys. J.* **C75** (2015) 79, doi:10.1140/epjc/s10052-014-3233-4, arXiv:1410.5404.

[6] J.-L. Agram et al., "Monotop phenomenology at the Large Hadron Collider", *Phys.Rev.* **D89** (2014) 014028, doi:10.1103/PhysRevD.89.014028, arXiv:1311.6478.

[7] I. Boucheneb, G. Cacciapaglia, A. Deandrea, and B. Fuks, "Revisiting monotop production at the LHC", *JHEP* **01** (2015) 017, doi:10.1007/JHEP01(2015)017, arXiv:1407.7529.

[8] CMS Collaboration, "The CMS experiment at the CERN LHC", *JINST* **3** (2008) S08004, doi:10.1088/1748-0221/3/08/S08004.

[9] CMS Collaboration, "Particle-flow reconstruction and global event description with the CMS detector", (2017). arXiv:1706.04965. Submitted to *JINST*.

[10] CMS Collaboration, "A Cambridge-Aachen (C-A) based Jet Algorithm for boosted top-jet tagging", Technical Report CMS-PAS-JME-09-001, CERN, 2009. Geneva, Jul, 2009.

[11] D. Berteloni, P. Harris, M. Low, and N. Tran, "Pileup per particle identification", *JHEP* **59** (2014) 059, doi:10.1007/JHEP10(2014)059, arXiv:1407.6013.

[12] CMS Collaboration, "Determination of jet energy calibration and transverse momentum resolution in CMS", *JINST* **6** (2011) 11002, doi:10.1088/1748-0221/6/11/P11002, arXiv:1107.4277.

[13] A. J. Larkoski, S. Marzani, G. Soyez, and J. Thaler, "Soft Drop", *JHEP* **05** (2014) 146, doi:10.1007/JHEP05(2014)146, arXiv:1402.2657.

[14] CMS Collaboration, "Identification of b-quark jets with the CMS experiment", *JINST* **8** (2012) P04013, doi:10.1088/1748-0221/8/04/P04013.

[15] CMS Collaboration, "Performance of b tagging at $\sqrt{s} = 8$ TeV in multijet, $\mathrm{t\bar{t}}$, and boosted topology events.", CMS Physics Analysis Summary CMS-PAS-BTV-13-001, 2013.

[16] J. Thaler and K. Tilburg, "Identifying boosted objects with N-subjettiness", *JHEP* **03** (2011) 015, doi:10.1007/JHEP03(2011)015, arXiv:1011.2268.

[17] C. Anders et al., "Benchmarking an even better top tagger algorithm", *Phys. Rev.* **D89** (2014) 074047, doi:10.1103/PhysRevD.89.074047, arXiv:1312.1504.

[18] I. Moult, L. Necib, and J. Thaler, "New Angles on Energy Correlation Functions", *JHEP* **12** (2016) 153, doi:10.1007/JHEP12(2016)153, arXiv:1609.07483.

[19] M. Cacciari, G. P. Salam, and G. Soyez, "The Anti-k(t) jet clustering algorithm", *JHEP* **04** (2008) 063, doi:10.1088/1126-6708/2008/04/063, arXiv:0802.1189.

[20] CMS Collaboration, "Particle–Flow Event Reconstruction in CMS and Performance for Jets, Taus, and $E_{\mathrm{T}}^{\mathrm{miss}}$", CMS Physics Analysis Summary CMS-PAS-PFT-09-001, 2009.

[21] CMS Collaboration, "Performance of reconstruction and identification of tau leptons in their decays to hadrons and tau neutrino in LHC Run-2", Technical Report CMS-PAS-TAU-16-002, CERN, Geneva, 2016.

[22] J. Alwall et al., "The automated computation of tree-level and next-to-leading order differential cross sections, and their matching to parton shower simulations", *JHEP* **07** (2014) 079, doi:10.1007/JHEP07(2014)079, arXiv:1405.0301.

[23] P. Nason, "A new method for combining NLO QCD with shower Monte Carlo algorithms", *JHEP* **11** (2004) 040, doi:10.1088/1126-6708/2004/11/040, arXiv:hep-ph/0409146.

[24] S. Frixione, P. Nason, and C. Oleari, "Matching NLO QCD computations with parton shower simulations: the POWHEG method", *JHEP* **11** (2007) 070, doi:10.1088/1126-6708/2007/11/070, arXiv:0709.2092.

[25] S. Alioli, P. Nason, C. Oleari, and E. Re, "A general framework for implementing NLO calculations in shower Monte Carlo programs: the POWHEG BOX", *JHEP* **06** (2010) 043, doi:10.1007/JHEP06(2010)043, arXiv:1002.2581.

[26] T. Sjöstrand et al., "An Introduction to PYTHIA 8.2", *Comput. Phys. Commun.* **191** (2015) 159, doi:10.1016/j.cpc.2015.01.024, arXiv:1410.3012.

[27] M. L. Mangano, M. Moretti, F. Piccinini, and M. Treccani, "Matching matrix elements and shower evolution for top-quark production in hadronic collisions", *JHEP* **01** (2007) 013, doi:10.1088/1126-6708/2007/01/013, arXiv:hep-ph/0611129.

[28] R. Frederix and S. Frixione, "Merging meets matching in MC@NLO", *JHEP* **12** (2012) 061, doi:10.1007/JHEP12(2012)061, arXiv:1209.6215.

[29] J. H. Kuhn, A. Kulesza, S. Pozzorini, and M. Schulze, "Electroweak corrections to hadronic photon production at large transverse momenta", *JHEP* **03** (2006) 059, doi:10.1088/1126-6708/2006/03/059, arXiv:hep-ph/0508253.

[30] S. Kallweit et al., "NLO electroweak automation and precise predictions for W+multijet production at the LHC", *JHEP* **04** (2015) 012, doi:10.1007/JHEP04(2015)012, arXiv:1412.5157.

[31] S. Kallweit et al., "NLO QCD+EW automation and precise predictions for V+multijet production", in *50th Rencontres de Moriond on QCD and High Energy Interactions La Thuile, Italy, March 21-28, 2015*. 2015. arXiv:1505.05704.

[32] S. Kallweit et al., "NLO QCD+EW predictions for V + jets including off-shell vector-boson decays and multijet merging", *JHEP* **04** (2016) 021, doi:10.1007/JHEP04(2016)021, arXiv:1511.08692.

[33] NNPDF Collaboration, "Parton distributions for the LHC Run II", *JHEP* **04** (2015) 040, doi:10.1007/JHEP04(2015)040, arXiv:1410.8849.

[34] GEANT4 Collaboration, "GEANT4: A Simulation toolkit", *Nucl. Instrum. Meth.* **A506** (2003) 250, doi:10.1016/S0168-9002(03)01368-8.

[35] CMS Collaboration, "CMS Luminosity Measurements for the 2016 Data Taking Period", Technical Report CMS-PAS-LUM-17-001, CERN, Geneva, 2017.

[36] CMS Collaboration, "Performance of Photon Reconstruction and Identification with the CMS Detector in Proton-Proton Collisions at sqrt(s) = 8 TeV", *JINST* **10** (2015) P08010, doi:10.1088/1748-0221/10/08/P08010, arXiv:1502.02702.

[37] CMS Collaboration, "Differential cross section measurements for the production of a W boson in association with jets in proton-proton collisions at $\sqrt{s} = 7$ TeV", *Phys. Lett.* **B741** (2015) 12, doi:10.1016/j.physletb.2014.12.003, arXiv:1406.7533.

[38] CMS Collaboration, "Measurement of the production cross section for a W boson and two b jets in pp collisions at $\sqrt{s}$=7 TeV", *Phys. Lett.* **B735** (2014) 204, doi:10.1016/j.physletb.2014.06.041, arXiv:1312.6608.

[39] CMS Collaboration, "Measurements of jet multiplicity and differential production cross sections of $Z+$ jets events in proton-proton collisions at $\sqrt{s} = 7$ TeV", *Phys. Rev.* **D91** (2015) 052008, doi:10.1103/PhysRevD.91.052008, arXiv:1408.3104.

[40] CMS Collaboration, "Measurement of the production cross sections for a Z boson and one or more b jets in pp collisions at sqrt(s) = 7 TeV", *JHEP* **06** (2014) 120, doi:10.1007/JHEP06(2014)120, arXiv:1402.1521.

[41] CMS Collaboration, "Observation of the associated production of a single top quark and a W boson in pp collisions at $\sqrt{s}$ =8 TeV", *Phys. Rev. Lett.* **112** (2014) 231802, doi:10.1103/PhysRevLett.112.231802, arXiv:1401.2942.

[42] CMS Collaboration, "Measurement of the ZZ production cross section and Z $\to \ell^+\ell^-\ell'^+\ell'^-$ branching fraction in pp collisions at $\sqrt{s}$ =13TeV", *Phys. Lett.* **B763** (2016) 280, doi:10.1016/j.physletb.2016.10.054, arXiv:1607.08834.

[43] CMS Collaboration, "Measurement of the WZ production cross section in pp collisions at $\sqrt{s}$ =13 TeV", *Phys. Lett.* **B766** (2017) 268, doi:10.1016/j.physletb.2017.01.011, arXiv:1607.06943.

[44] CMS Collaboration, "Performance of the CMS missing transverse momentum reconstruction in pp data at $\sqrt{s}$ = 8 TeV", *JINST* **10** (2015) P02006, doi:10.1088/1748-0221/10/02/P02006, arXiv:1411.0511.

[45] A. L. Read, "Presentation of search results: The CL(s) technique", *J. Phys.* **G28** (2002) 2693, doi:10.1088/0954-3899/28/10/313.